

The Characterization of a 34-Meter Beam-Waveguide Antenna at Ka band (32.0 GHz) and X band (8.4 GHz)

David D. Morabito

Jet Propulsion Laboratory
California Institute of Technology
Pasadena, California
Tel: +1 (818) 354-2424
Fax: +1 (818) 393-4643
E-mail: ddm@rodan.jpl.nasa.gov

Keywords: Beam waveguides; satellite communication earth terminals; multireflector antennas; reflector antenna feeds; reflector antennas; space vehicle communication

1. Abstract

New antennas for the NASA Deep Space Network (DSN) have been built to replace the aging antennas of older designs for deep-space communications. These new antennas incorporate a new dual-shape design as well as a beam waveguide (BWG), which utilize a series of additional secondary mirrors to relocate the focal point into a stationary room below the main reflector. The advantages of using such a design include increased isolation of the feed package from outside environmental factors, such as moisture, wind, and temperature changes; and ease of access to the equipment for maintenance, troubleshooting and repair purposes.

This article reports on the performance of a beam waveguide antenna at X-band and Ka-band microwave frequencies. The Ka-Band Antenna Performance Experiment (KaAP) antenna-efficiency measurements presented in this article were acquired at the Goldstone DSS-13 Research and Development (R&D) beam-waveguide antenna between December, 1993, and November, 1995.

The measured antenna efficiency and ground-station figure-of-merit (gain divided by operating system noise temperature) as a function of elevation angle and their uncertainties are presented. Also described are the station configuration, the measurement technique, the modeling used in the analysis processing, and the historical evolution of the DSS-13 Ka-band antenna-efficiency measurements as progressive improvements and configuration changes were implemented.

2. Introduction

The beam-waveguide (BWG) design feature had been in use for several years for communications-satellite terminals, where ease of service outweighed the added noise due to the additional mirrors. However, for NASA Deep Space Network (DSN) usage, the concern for the added noise initially kept such antennas out of contention. In 1985, a team of JPL researchers worked in collaboration with Japan's Institute for Space and Astronautic Sciences (ISAS) to install one of JPL's experimental low-noise amplifiers into the ISAS 64-m BWG antenna in Usuda, Japan. This configuration was demonstrated at S band (2 GHz), using the International Cometary Explorer (ICE) spacecraft, achieving good performance with no significant noise penalty. Moving from this demonstration to application of the BWG technology in the DSN resulted in the

building of the prototype DSS-13 antenna. The completed antenna operated effectively at 2, 8, and 32 GHz [1].

Several DSN telecommunications studies have shown that by utilizing Ka-band (31.8 to 32.3 GHz) frequencies in place of X band (8.40 to 8.45 GHz) on a spacecraft-to-ground communications link, an advantage of approximately 7 dB (a factor of five improvement) can be realized for a given spacecraft transponder weight, antenna size, and power allocation [2, 3]. The link advantage can be used to increase data volume, decrease transmission time, decrease transmitter power on the spacecraft, decrease spacecraft antenna size, or allow for a smaller antenna on the ground. The increased advantage comes from increased antenna gain at the shorter wavelengths. However, in practice, the advantage is reduced by higher atmospheric noise, antenna performance deficiencies, and weather susceptibility at Ka band.

The concept of conducting a Ka-band link experiment to verify these studies, and to discover any impediments that could deter this performance gain from being realized, was proposed by Riley et al. in 1987 [4]. The first Ka-band link experiment at 33.7 GHz became reality with the Mars Observer Project's KaBLE (Ka-Band Link Experiment), which acquired data at DSS-13 from Mars Observer's Ka-band beacon and X-band signal between January and August, 1993 [5].

With the loss of Mars Observer in August, 1993, it became important to find other ways to continue the study of the link advantage, until another spacecraft with Ka-band capability became available. The KaAP (Ka-band Antenna Performance Experiment) Project was initiated in December, 1993, to evaluate antenna efficiency by observing natural radio sources at both Ka band and X band. These evaluations allow the characterization of the antenna efficiency at each frequency band as incremental performance improvements and configuration changes are realized. The ground-station advantage of Ka band relative to X band is quantified using the acquired data from both bands. The effort also facilitates the demonstration and development of optimal operational strategies for BWG antennas. The information gained is of benefit to the DSN and flight projects that may be considering Ka band for their telecommunications-link carrier frequency. The knowledge gained about the temporal variability of the Ka-band advantage due to weather effects allows planners of future flight projects to develop robust, efficient telecommunication strategies at Ka band.

Since the loss of Mars Observer in 1993, Ka-band data have been acquired from two additional spacecraft. SURFSAT-1, launched on November 4, 1995, was a DSN Technology Program flight experiment. SURFSAT-1 tracking data were acquired

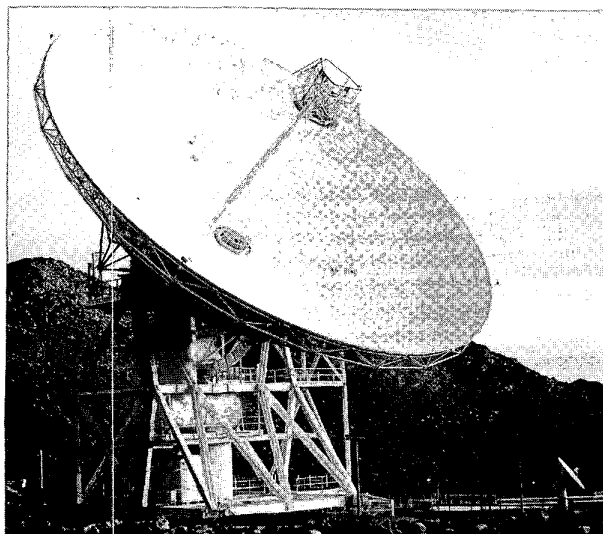


Figure 1. A Photograph of the 34-m beam-waveguide antenna, DSS-13, located at the Goldstone Deep Space Communications Complex, near Barstow, California.

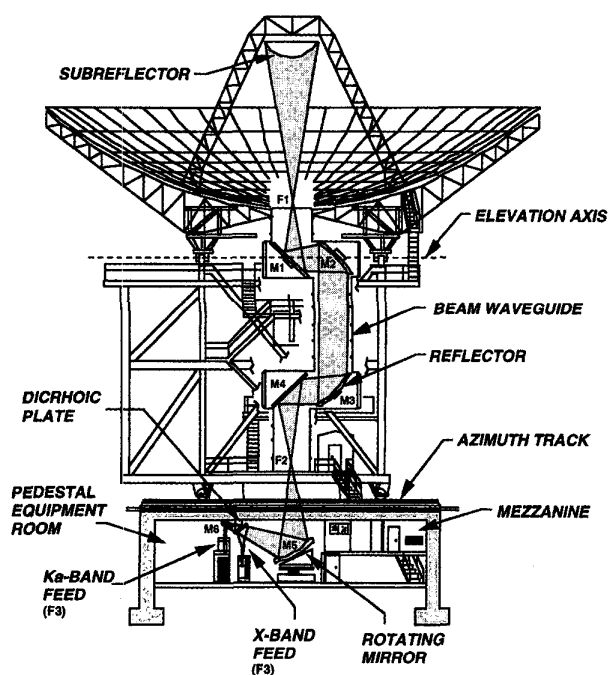


Figure 2. A geometric-configuration diagram of the reflectors and mirrors on the DSS-13 BWG antenna, along with the locations of the focal points.

between launch, in November, 1995, and December, 1996, for the purpose of characterizing this link advantage. Mars Global Surveyor, launched in November, 1996, carries KaBLE-II, another DSN Technology Program experiment. MGS KaBLE-II Ka-band data are currently being acquired at DSS-13, and preliminary results have been published [6, 7]. These missions allow Ka-band link-advantage studies to continue, using X-band and Ka-band spacecraft signal sources. In October, 1998, another spacecraft with

Ka-band capability, DS1, was launched. DS1 Ka-band data-acquisition activities were expected to start early in 1999.

This article focuses on the antenna-efficiency characterization of the DSS-13 BWG antenna, using natural radio-source observations. The DSS-13 R&D beam-waveguide antenna and system used for the measurements are described in Section 3. The data-acquisition technique and model used in the analysis are described in Section 4. The results are presented and discussed in Section 5.

3. Ground station and equipment

Figure 1 is a photograph of the DSS-13 beam-waveguide antenna. The beam-waveguide tubing, which guides the signal power to the subterranean pedestal room, is clearly prominent.

The locations of focal points, mirrors, and feed packages are displayed in the schematic cartoon of Figure 2. The "optical" ray traces of the signals as they propagate are depicted by the shaded path from the subreflector to the Ka-band feed. The signal energy is collected by the main reflector and subreflector, and focused at F1. Reflector mirrors M1 through M4 guide the signal to the rotating-ellipsoid focus at F2. The signal is then scattered off the ellipsoidal mirror, M5. The X-band signal energy is reflected off the dichroic plate, focused at the other focal point of the ellipsoidal mirror, and received in the X-band feed-horn package.

The Ka-band signal energy is guided through the beam waveguide in the same manner as the X-band signal, except that after scattering off the ellipsoid, the shorter wavelength Ka-band signal passes through the dichroic plate. It is then reflected off an additional mirror (M6), mounted in the ceiling, and is focused at the other focal point of the ellipsoid and received by the Ka-band feed horn in the Ka-band package [8].

Figure 3 is a photograph of the center ellipsoidal mirror, and several of the surrounding feed packages located in a concentric ring in the subterranean pedestal room. The center ellipsoidal mirror can be rotated to select among any of these feed packages, each of which utilizes different frequencies and modes of operation, cor-

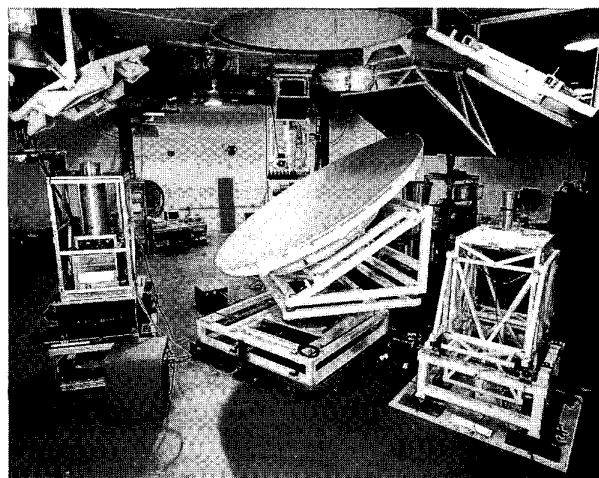


Figure 3. A photograph of the interior subterranean pedestal room, showing the center ellipsoidal mirror and surrounding feed packages.

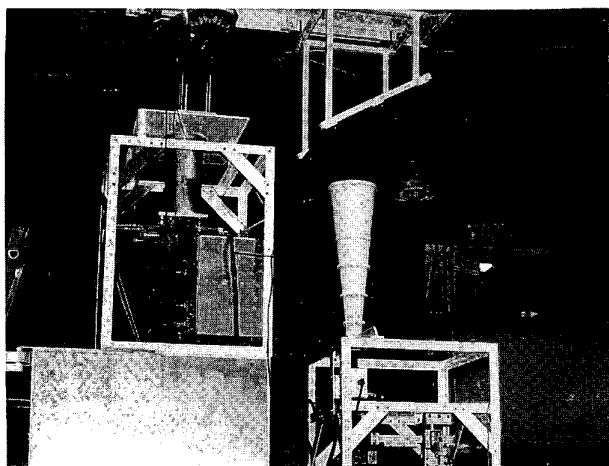


Figure 4. A photograph of the KaAP X-band and Ka-band feed packages and the X/Ka dichroic plate, along with a portion of the center ellipsoidal mirror.

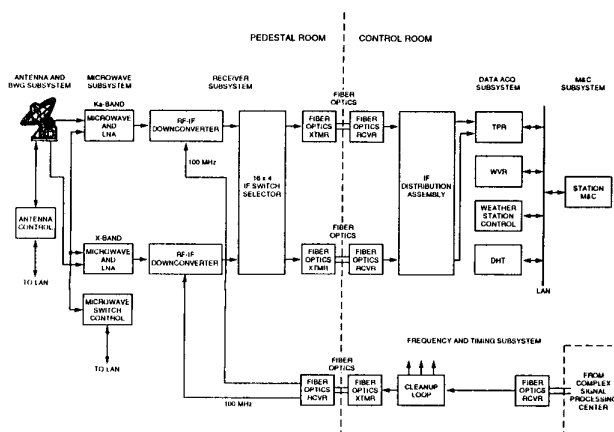


Figure 5. A block diagram of the DSS-13 station configuration used for the experiments. See page 22 for an enlarged version of this figure.

responding to its scientific or engineering purpose. Figure 4 is a close-up view of the feed packages used for the X-band and Ka-band experiments discussed in this article.

The ground station can be broken into several subsystems: antenna, microwave, receiver, data acquisition, monitor and control (M&C), and frequency and timing (FTS), each of which will be discussed in the following subsections. Figure 5 displays a block diagram of the station configuration used for these experiments.

3.1 Antenna subsystem

The antenna at Ka band (17 mdeg HPBW: half-power beam-width, which is defined as the full width between the half-power points of the antenna beam) requires more-accurate pointing when tracking objects than it does at X band (63 mdeg HPBW). Whereas an accuracy of 8 mdeg for X band is sufficient, for Ka-band pointing, errors must be kept within 3 mdeg, to limit pointing loss to under 0.5 dB. In the past, pointing calibrations had been shown to correct errors to about 5 mdeg rms in a blind or open-loop mode.

Further reduction of pointing errors is realized using an automatic boresight technique, which corrects pointing over five-minute (typical) measurement periods [9].

Typical pointing corrections from this technique, called AUTOBORE, are accurate to within 1 to 2 mdeg rms. Since pointing corrections are continually updated during successive observations of the same radio source, there is no systematic loss due to beam-pointing errors.

Systematic losses due to subreflector focusing and BWG mirror misalignments may be present at some level. These effects are reflected in the measured antenna efficiency versus elevation angle curves, which may differ for different radio-source declinations.

The overall contribution of the antenna reflectors and BWG mirrors to the noise temperature is about 9.5 K at Ka band, and 7 K at X band.

3.2 Microwave subsystem

The microwave subsystem takes advantage of the pedestal room layout to allow switching among different feed packages, arranged in a ring around a center rotating ellipsoidal reflector (see Figure 3). The feed package used for KaAP (see Figure 4) consists of an X/Ka dichroic plate, a 25 dBi horn for X band, a 26 dBi horn for Ka band, and high-electron-mobility transistor (HEMT) low-noise amplifiers (LNA) for both bands.

The X/Ka dichroic plate allows simultaneous reception of X-band (8.4 GHz) and Ka-band (32 GHz) signals (see Figures 6a and 6b). The plate passes the higher-frequency Ka-band circularly polarized signals with low insertion loss, while at the same time reflecting the lower-frequency X-band signals. The dichroic plate is a copper metallic plate (Figure 6a) that is perforated with rectangular apertures (Figure 6b). An oblique angle of incidence is required, due to mechanical constraints. A skew grid is employed for bandwidth considerations. The plate employs a 5.08 mm by 5.156 mm rectangular aperture, a 60° skew angle, and a 9.271 mm plate thickness. The elliptical perforated area of the plate is 561.848 by 444.5 mm. The conductivity loss of the rough surface, together with the addition to the reflected energy from the horn pattern, contributes about 1.3 K to the overall noise temperature at 32.0 GHz. The dichroic plate is described in more detail by Chen et al. [10].

The Ka-band feed package includes a 26.1 dBi horn that is an extension of a 22 dBi corrugated horn, followed by a waveguide window. The feed-horn window is composed of Kapton. An ellipsoidal reflector mirror is located above the 32 GHz feed. The cooled components include a round-to-square-transition copper thermal isolator, followed by a copper polarizer, a cross-guide coupler, a copper isolator, and a WR-28 copper waveguide going into the LNA. The LNA utilizes four stages of General Electric and Fujitsu transistors in an amplifier of National Radio Astronomy Observatory design, with a total noise temperature of about 28 K.

Compressed helium gas is used to cool the LNA/waveguide-feed packages in closed-vessel systems, using closed-cycle refrigerators. The interior of the housing is kept in a vacuum. The LNAs are cooled by thermally connecting them to the closed-cycle-refrigerator cold station to physical temperatures below 20 K, which are thermally stabilized [11].

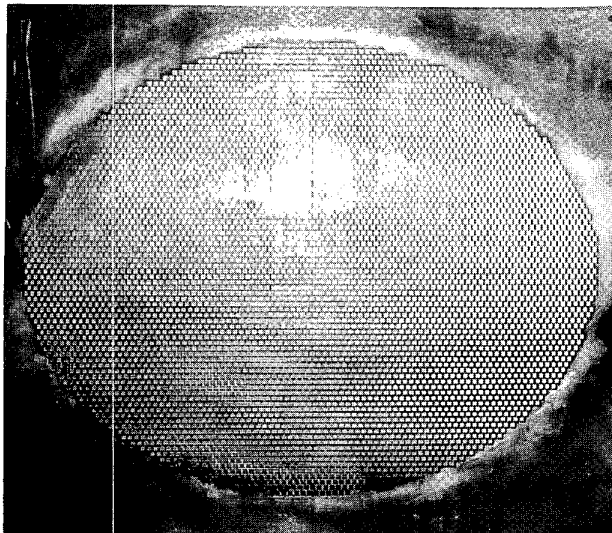


Figure 6a. A photograph of the dichroic plate used for simultaneous reception of X-band and Ka-band signals.

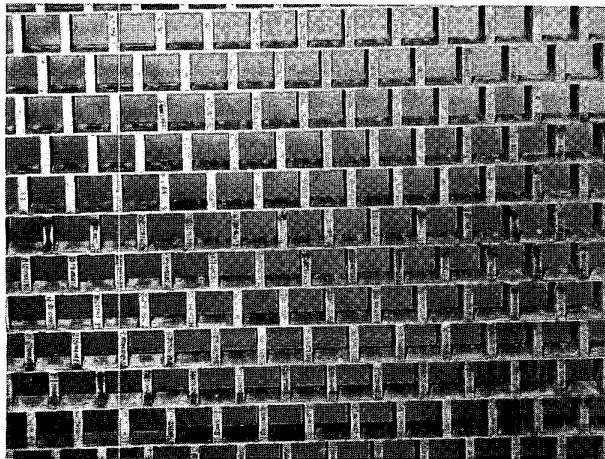


Figure 6b. A close-up of the rectangular apertures in the dichroic plate shown in Figure 6a.

The loss factor of the cooled waveguide/feed package is estimated to be about 0.325 dB at Ka band. After adding room-temperature contributions due to window and horn, this results in an overall package loss of about 0.4 dB, for a noise temperature contribution of about 5 K. The resulting estimated temperature of the total package is about 32 K, in reasonable agreement with measurements of 34 K [11].

At X band, HEMT devices were also used for the LNA. The LNA and ambient-temperature feed components combine for an overall noise-temperature contribution of about 28 K for the full package.

For 32 GHz, an ambient load is swung over the horn during noise calibrations. For the 8.4 GHz system, a waveguide switch, located in front of the LNA, is used. Both ambient loads have embedded temperature sensors, used to provide data for input to

the calibration algorithms. Both systems employ noise diodes which, together with the ambient loads, allow system linearity to be measured (see Section 3.4).

The outputs of the LNAs are connected to an isolator, which connects to the bottom plate of the vacuum vessel. This, in turn, connects to the external downconverter assembly, which consists of follow-up filters and amplifiers.

3.3 Receiver subsystem

The receiver subsystem used for both frequency bands consists of RF-to-IF downconverters, an IF switch selector, fiber-optic links from the pedestal room to the control room, and an IF distribution assembly in the control room.

The X-band down-conversion is performed using an 8.1 GHz first local oscillator (LO). The bandwidth of the second IF filter is 500 MHz.

For Ka band, two configurations have been used. During the 33.7 GHz data-acquisition period (from December, 1993, to October, 1994), the incoming 33.7 GHz signal was mixed with a 25.2 GHz first LO, followed by an 8.2 GHz second LO. The bandwidth of the second IF filter was 100 MHz. For the 32.0 GHz data-acquisition system, installed in late 1994, the incoming 32.0 GHz signal was mixed with a 23.6 GHz first LO, followed by an 8.1 GHz second LO. The bandwidth of the second IF filter was 500 MHz. All LOs are coherent with the station frequency and timing subsystem (FTS).

The downconverter-output X-band and Ka-band IF signals are fed into a switch selector, which connects them to the fiber-optic system. The IF signals are converted to optical signals, and transmitted over fiber-optic links from the pedestal room to the control room, where they are converted back to IF. The IF signals are fed to an IF-distribution assembly (amplifiers and power dividers), where they are distributed to other subsystems in the control room.

3.4 Data-acquisition subsystem

The instruments included in this subsystem include the total-power radiometer (TPR), used for measuring T_{op} ; the water-vapor radiometer (WVR), for measuring atmospheric noise; the weather station; and the data-handling terminal (DHT) used for displaying and recording data to disk.

The TPR operates together with the microwave switch controller (USC) to provide calibrated T_{op} measurements during the track. The two incoming IF channels are filtered (20 MHz for X band and 30 MHz for Ka band) to limit the incoming noise bandwidth and any RFI. The bandwidth of these filters, together with the radiometer integration time (5 sec), define the contribution of the receiver noise for the T_{op} measurements, which lies below 0.01 K for both systems. Variable-step attenuators are used to set the power levels to a 1 microwatt level when the LNA input is on the ambient load with the noise diode on. Measurements of the total IF noise power are made with two HP8481 power sensors, followed by HP437B or HP438A power meters: one each for X band and Ka band. The power sensors operate from 10 MHz to 18 GHz within 100 picowatt to 10 microwatt power values. A local

computer platform reads these measurements and converts them to T_{op} values, based on the transfer function derived from each calibration.

Calibrations are performed regularly throughout each track, alternating with the boresight observations. An initial set of calibrations at zenith is always performed at the beginning of a track (known as a PRECAL), and sometimes at the end of a track (known as a POSTCAL). During each calibration, the total-power radiometer measures the total IF noise power, while the HEMT input is switched from (1) sky, to (2) sky plus noise diode, to (3) ambient load, to (4) ambient load plus noise diode. The measurements are converted into a transfer function (T_{op} versus total noise power), and also allow for the correction of any non-linearity that may be present. A detailed discussion of the system-calibration methodology is presented by Stelzried and Klein [12].

The water-vapor radiometer is a small, stand-alone microwave radiometer package, positioned near the antenna. It measures the noise-temperature contribution of water in the atmosphere, in vapor and liquid form [13]. The water-vapor radiometer measures sky temperatures at 20.7 GHz and 31.4 GHz, over effective bandwidths of 320 MHz. It consists of a platform with a small feed horn and mirror assembly that can observe any point in the sky with a beamwidth of 7°. Comparisons of water-vapor-radiometer-derived atmospheric noise temperatures with those derived from BWG total-power radiometer data have yielded consistent results [14].

A "weather system" samples and records a range of meteorological parameters, including atmospheric pressure, air temperature, relative humidity, wind speed, and wind direction. These measurements are input to a program that estimates atmospheric-noise temperature and attenuation, based on a surface model.

3.5 Monitor and control subsystem

All of the subsystems are linked together into an operational system with a high degree of flexibility, known as the Monitor and Control (M&C) subsystem. Data have been acquired using Monitor and Control systems that ran on '486 PC and SUN workstation platforms. Interfacing to the other subsystems is provided by the local area network (LAN).

3.6 Frequency and timing subsystem

For frequency and timing, all of the sensitive reference-frequency distributions are made using optical fiber. Optical fiber is also used in the transmission of the broadband IF signals from the pedestal room to the control room. Fiber optics have improved stability over that of coaxial cable.

4. Data acquisition and analysis

Since the KaAP data acquisition began in December, 1993, after the end of the Mars Observer KaBLE experiment, the antenna efficiency measurements were acquired on a routine basis. Each time a configuration change was implemented, the performance determined from the new set of measurements was compared with

that of the previous configuration. Any resulting change in antenna efficiency was compared with available predictions.

The efficiency measurements were acquired using the receivers located in the subterranean pedestal room of DSS-13, where the incident energy was channeled from the antenna's main reflector and subreflector using a series of beam waveguides and mirrors. In the pedestal room, the feed position consisted of equipment for receiving two simultaneous wavelengths, one at 8.425 GHz (X band) and one at 32.0 GHz/33.7 GHz (Ka band), as described in Section 3. The observation strategy, the model used to process the data, the observed radio sources, and estimated uncertainties will be described here.

4.1 Description of measurement sequence

KaAP uses dual frequency observations of natural calibrator radio sources at Ka band (33.7 GHz and 32.0 GHz) and X band (8.425 GHz), producing estimates of the antenna efficiency at each frequency. Each track or experiment consists of a series of radio-source observations distributed over different parts of the sky, over a wide elevation-angle range. There were typically one to two tracks per month, with each lasting eight to 24 hours in duration. Each track consists of (1) a series of boresight observations of different radio sources, (2) a series of radiometer calibrations, and (3) tipping curves (measurements of cold-sky temperature versus elevation angle, from zenith to near horizon). The boresight observations alternate with the calibrations during the main body of the pass, with tipping curves usually performed at the start of, or the end of, the pass.

A sequence of an X-band boresight, a Ka-band boresight, and radiometer calibrations at both X band and Ka band were performed for each measurement cycle of a source, when the KaAP effort first started. Afterwards, the tracks consisted of either Ka-band-only or X-band-only boresight observations, alternating with the calibrations.

4.1.1 Boresight observations

Each boresight observation of a radio source involves stepping the antenna beam across the radio source, while taking system operating noise temperature measurements (T_{op}), using the total-power radiometer. A peak noise temperature due to the source is estimated by fitting a linearized Gaussian beam model [9] over the T_{op} measurements, in two orthogonal directions across the radio source: in cross-elevation (XEL) and in elevation (EL). The model is fitted over the a-priori on-source point (0 dB), the half-power-down (-3 dB) points, and off-source points. The solution yields the peak noise temperature due to the radio source, ΔT_{pk} ; an estimate of the half-power beamwidth (θ_{HP}); and an estimate of the pointing correction relative to the accumulated pointing correction just prior to the boresight observation, $\Delta\theta$; in each direction.

The peak source noise temperatures are converted into estimates of antenna efficiency using the radio source's catalogued flux density, and corrections for the angular flux distribution over the antenna beam, estimated atmospheric attenuation (to refer the measurements to zero atmosphere), and any system non-linearity that may be present.

4.1.2 System calibrations

Radiometer calibrations are routinely conducted to correct for gain changes as the experiment progresses, and to allow the system non-linearity to be determined. The radiometer calibrations were described in Section 3.4.

4.1.3 Tipping curve measurements

In addition to the boresight observations and system calibrations, a sequence of tipping curve observations is routinely performed to characterize the atmosphere. These provide a means of determining the atmospheric loss factor used to refer the antenna-efficiency measurements to zero atmosphere, and the atmospheric noise temperature used for statistical cross-comparisons with independent water-vapor-radiometer and surface-model estimates.

The tipping curves were usually done at the start or end of a pass, with each lasting about 30 minutes. The tipping-curve acquisition consists of a set of cold-sky T_{op} measurements at elevation angles that ranged from near horizon to zenith. Normally, the atmosphere is sampled from 1 airmass (zenith) to about 4 airmasses (14.5° elevation angle).

4.2 Description of antenna-efficiency model

Given a radio source of known flux density, the increase in system operating noise system temperature (T_{op}), as determined by the boresight measurements (peak source noise temperature fitted over a linearized Gaussian model), is a measure of the antenna efficiency. The antenna-efficiency measurement for the BWG antenna is referenced to the plane where the ambient load is inserted during calibrations. This measurement accounts for power losses of the main reflector, subreflector, BWG mirrors, dichroic plate, and any feed package loss, including the waveguide up to the ambient load plane. For X band, the antenna efficiency is referred to the input of the HEMT, where an ambient load is inserted by a waveguide switch during calibrations. For Ka band, the antenna efficiency is referred to the input of the feed horn, where an ambient load is swung over it during calibrations.

Given one received component of a randomly polarized radio source, the flux density is given by

$$S = \frac{2k\Delta TC_r C_p}{A_e}, \quad (1)$$

where S is the radio-source flux density, W/(m²-Hz); ΔT is the radio-source noise temperature increase one would measure in a vacuum (K); A_e is the effective area of the antenna (m²); C_r is the source-size correction; C_p is the pointing correction; and k is Boltzmann's constant (1.38062×10^{-23} W/(K-Hz)).

The source-size correction, C_r , accounts for extended structure over the antenna beam, and is equal to 1.0 for a point source. A standard unit for flux density, S , is the Jansky (Jy) (1 Jy = 10^{-26} W/m²-Hz). The pointing correction, C_p , is equal to 1.0 when there is no mispointing.

The AUTOBORE program performs sequential cross-elevation (XEL) and elevation (EL) cuts of a radio source. The meas-

ured increases in system operating noise temperature, due to a radio source are ΔT_{xel} and ΔT_{el} in the cross-elevation and elevation directions, respectively.

The best estimate of the source noise-temperature increase, ΔT_m , is the average

$$\Delta T_m = \frac{\Delta T_{xel} + \Delta T_{el}}{2}. \quad (2)$$

In order to estimate the antenna efficiency one would measure in a vacuum, the source-noise temperature measurements, ΔT_m , are corrected by the atmospheric loss factor, $L_{atm}(\theta)$. The tipping curve data were used to determine $L_{atm}(\theta)$. Hence, ΔT is estimated from ΔT_m (Equation (2)) using

$$\Delta T = L_{atm}(\theta) F_{lin} \Delta T_m, \quad (3)$$

where F_{lin} is the system linearity factor, determined from the radiometer calibration data. For Goldstone, typical zenith values of attenuation— $10 \log(L_{atm})$ —as determined by the tipping-curve measurements are 0.035 dB at X band, and 0.15 dB at Ka band.

Given that the effective area of the antenna is related to the antenna efficiency, ε , and antenna diameter, D (m), by

$$A_e = \frac{\varepsilon \pi D^2}{4}, \quad (4)$$

we can relate ε to the other parameters by combining Equations (1), (3), and (4) as follows:

$$\varepsilon = \frac{8k\Delta TC_r C_p}{\pi D^2}. \quad (5)$$

Another measure of antenna performance is the figure-of-merit, G/T_{op} , or the effective gain of the antenna, G , divided by the system operating-noise temperature, T_{op} . Since G/T_{op} is used for spacecraft-to-ground link studies, the effects of the atmospheric loss are included, so that variations over a wide range of atmospheric conditions can be studied.

The effective gain, G , is related to ε by

$$G = \frac{\varepsilon}{L_{atm}} \left(\frac{\pi D}{\lambda} \right)^2, \quad (6)$$

where D is the antenna diameter (m) and λ is the observing wavelength (m). Therefore,

$$\frac{G}{T_{op}}(\theta) = \frac{\varepsilon(\theta) \pi^2 D^2}{L_{atm}(\theta) T_{op}(\theta) \lambda^2}. \quad (7)$$

T_{op} includes all contributions seen by the antenna (including cosmic, atmosphere, main structure and mirrors, feed package, amplifier, and follow-on equipment). Typical zenith values of T_{op} at the KaAP feed position were 40 K at 8.4 GHz and 55 K at 32 GHz.

4.3 Radio source calibrators

The flux densities, their uncertainties, and the source-size correction factors of the observed natural radio sources have been derived from independent studies, and are listed in Table 1. The 8.4 and 32 GHz values for 3C274 and DR21 are from Richter [15], and the values given for the variable source 3C84 are nominal baseline values. The tabulated C_r values assume a 34 m antenna with HPBW of 63 mdeg for 8.42 GHz, and 16.8 mdeg for 32 GHz.

The radio galaxy 3C274 (also known as M87 and Virgo A) is used as the principal calibrator at X band and Ka band. This source establishes the peak flux density near 45° elevation, as well as the curve shape over a wide elevation-angle range. Since 3C274 is a low-declination source, a higher-declination source, 3C84, is normally used to supplement the measurements. Since 3C84 is a variable radio source, it is primarily used for elevation-angle curve-shape information at the higher declination. The computed efficiencies for 3C84 (using the baseline flux-density values of Table 1) are scaled such that its peak antenna efficiency matches that of the 3C274 data for each pass.

The determination of S and C_r for the planets Jupiter and Venus depend on additional parameters. The flux density, S , is related to the disk-brightness temperature (see Table 2) at each observing wavelength, λ , as follows:

$$S = \frac{2kT_B\Omega}{\lambda^2}, \quad (8)$$

where T_B is the blackbody disk temperature (K), Ω is the solid angle subtended by the planet ($\pi D_p^2/4\rho^2$), D_p is the geometric mean of the planet diameter (km), and ρ is the distance to the planet (km).

Table 1. Extragalactic radio sources used for efficiency calibration.

Source	Frequency (GHz)	S (Jy)	σ_s/S (%)	C_r	Ref.
3C274	8.425	44.69	2.4	1.087	[15]
	32.0	16.22	3.1	1.270	[15]
	33.7	15.62	3.1	1.270	[28]
DR 21	8.425	19.47	2.3	1.004	[15]
	32.0	18.2	2.3	1.05	[15]
3C84	8.425	24.0	—	1.0	Baseline
	32.0/33.7	15.1	—	1.0	Baseline

Table 2. Brightness temperatures of the planets.

Planet	Frequency (GHz)	T_B (K)	σ_{TB}/T_B (%)	Ref.
Venus	8.4	652	2.3	[17]
	32.0	467	4	[17]
	33.7	461	4	[17]
Jupiter	8.4	210	4	[19]
	32.0	154	5	See text
	33.7	152	5	[29]

The source-size correction factor for a planet, assuming uniform brightness and a Gaussian antenna beam, is given by [16]

$$C_r = \frac{\ln 2Q^2}{(1 - 2^{-Q^2})}, \quad (9)$$

where

$$Q = 2\sqrt{\frac{R_{eq}R_{pol}}{\rho\theta_{HP}}}, \quad (10)$$

and where θ_{HP} is the half-power beamwidth of the antenna in radians, and R_{eq} and R_{pol} are the equatorial and polar radii of the planet, respectively. For Venus, $R_{eq} = R_{pol} = 6120$ km. For Jupiter, $R_{eq} = 71492$ km and $R_{pol} = 66854$ km.

The Ka-band brightness temperatures for Venus in Table 2 were extrapolated from a spectral curve given in Steffes, Klein, and Jenkins [17]. For Jupiter, an appropriate blackbody correction was applied to the 33.7 GHz 152 K value at 33.7 GHz to get 154 K at 32.0 GHz.

Because of larger measurement discrepancies relative to 3C274, the planets have not been routinely observed as calibration sources. Earlier observations of Venus and Jupiter are discussed in Section 5.

4.4 Antenna efficiency error contributions

The uncertainty in the antenna-efficiency measurements can be estimated using

$$\sigma_\varepsilon(\theta) = \varepsilon(\theta) \sqrt{\left(\frac{\sigma_S}{S}\right)^2 + \left(\frac{\sigma_{\Delta T_m}}{\Delta T_m}\right)^2 + \left[\frac{\sigma_{L_{atm}}(\theta)}{L_{atm}(\theta)}\right]^2 + \left(\frac{\sigma_{C_p}}{C_p}\right)^2}, \quad (11)$$

where σ_S/S is the uncertainty of the source-flux density, $\sigma_{\Delta T_m}/\Delta T_m$ is the uncertainty of the source noise-temperature measurement, $\sigma_{L_{atm}}/L_{atm}$ is the uncertainty of the atmospheric loss factor, and σ_{C_p}/C_p is the uncertainty due to any mispointing.

The values of σ_S/S are given in Table 1 for the extragalactic radio sources, and can be inferred from σ_{T_B}/T_B in Table 2 for the planets. This contribution defines the absolute calibration error for the measurements.

The uncertainty $\sigma_{\Delta T_m}$ is an estimate of the noise temperature measured by the radiometer during the measurement period. Typical uncertainties for 3C274 at Ka band are about 0.1 K ($\Delta T_m \sim 2.3$ K). The main contributors are expected to be gain instability and atmospheric noise during the AUTOBORE measurement period. This term dominates the observed scatter of the measurements during a pass.

The atmospheric loss factor uncertainty, $\sigma_{L_{atm}}$, can be estimated from the expected variation of the atmospheric noise temperature over a pass. Because the tipping curves are usually per-

formed once per pass (not during the AUTOBORE measurements), L_{atm} is effectively a nominal estimate over the pass. Long-term variations in atmospheric attenuation over a pass thus define $\sigma_{L_{atm}}$, while short-term variations (within the period of the boresight measurement) would be manifested in $\sigma_{\Delta T_m}$.

Losses due to beam-pointing errors, σ_{C_p} , are expected to be small, since AUTOBORE is continually updating the pointing corrections. It is possible that errors due to mispointing may be as high as 0.5%, which still lie below those attributed to radiometer and atmospheric noise. Systematic losses due to errors in sub-reflector focusing and beam-waveguide mirror misalignments will be reflected directly in the antenna-efficiency measurements. Data acquired at other feed positions may have different peak efficiencies and elevation-dependent curve shapes because of such misalignments.

5. Results

Figure 7 displays the measured antenna efficiencies at X band and Ka band versus elevation angle for data acquired from February to November, 1995, at the KaAP X/Ka-band feed position. The X-band data will be discussed in Section 5.1, and the Ka-band data will be discussed in Section 5.2. Also discussed will be G/T performance (Section 5.3), and a history of DSS-13 Ka-band performance improvements (Section 5.4).

The antenna-efficiency measurements, Equation (5), gathered from different radio sources and different passes for a given frequency band, and the station configuration are combined into a common data set. An antenna efficiency versus elevation angle curve is then least-squares fit to the data, using a second-degree polynomial model:

$$\varepsilon(\theta) = c_0 + c_1\theta + c_2\theta^2, \quad (12)$$

where the c_i , $i = 1, 2, 3$, are the solved-for coefficients, and θ is the elevation angle of the observation.

Table 3 lists the fitted coefficients of a second-degree polynomial, using Equation (12), over the X-band and Ka-band data referenced to the F3 focal point (see Figure 2).

5.1 Antenna efficiency measurements: X band at F3

Provided in Figure 7 are the data points with estimates of the error bars (excluding the absolute error contribution of the flux density), and the best-fit curve for X-band data acquired between February through May, 1995. The rms error of the data points about the best-fit curve is 0.9% over 77 observations. The measured peak antenna efficiency is 71.1% at 37° elevation, which is in agreement with the 71.8% predicted value, based on estimates of individual contributors [19].

A comparison of the measured KaAP X-band antenna efficiency was in good agreement with that measured at another X-band feed system at DSS-13 by Imbriale, Esquivel, and Manshadi [8]. After backing out estimated contributions of the feed packages, the X-band efficiencies referred to common antenna hardware were 75.5% at the S/X feed position, and 75.9% at the KaAP feed position.

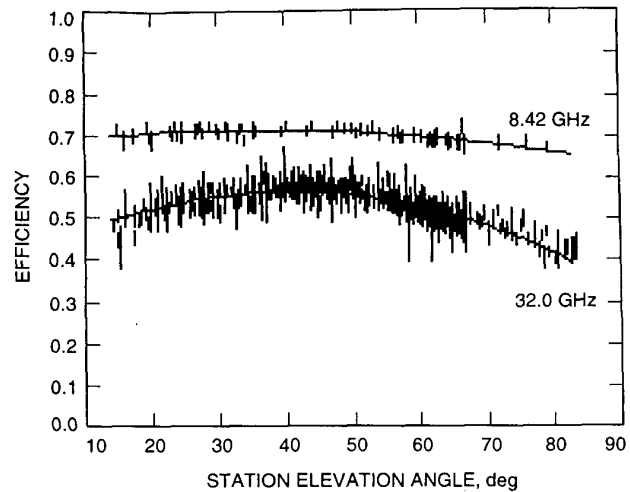


Figure 7. The antenna efficiency as a function of the elevation angle of the DSS-13 BWG antenna at X band (8.4 GHz) and at Ka band (32.0 GHz), along with error bars and best-fit curves.

Table 3. The best-fit second-degree polynomial coefficients for DSS-13 X-band and Ka-band efficiencies (at F3, no atmosphere).

	c_0	c_1	c_2	ε_{pk} (%)	θ_{pk} (deg)	
X band	0.675662	0.0019537	-0.000026679	71.1	36.6	All Data
Ka band	0.344228	0.0111526	-0.000136727	57.1	40.8	3C274
Ka band	0.378161	0.0085412	-0.000097117	56.3	44.4	3C84
Ka band	0.409153	0.0075158	-0.000091870	56.2	41.1	All Data

The X-band brightness temperatures of the planets Jupiter and Venus in Table 2 produced results (using earlier 1994 data) that were in reasonable agreement with those of 3C274. The peak X-band antenna efficiency using Venus-only data was 2.1% lower than that of the 3C274-only data, but still within the 2.3% uncertainty given in Table 2. The X-band antenna efficiency using Jupiter-only data was within 0.1% of the efficiency computed using 3C274-only data.

5.2 Antenna efficiency measurements: Ka band at F3

Figure 7 also displays the antenna efficiency at 32.0 GHz (Ka band) versus elevation angle in the form of the data points with estimated error bars (excluding the absolute error contribution in flux density), and the best-fit curve over the data acquired from February to November, 1995. The rms of the data points about the best-fit curve is 1.9% over 444 total observations. The measured peak antenna efficiency of the 3C274-only data points (321 observations) is 57.1% at 40.8° elevation, which is in agreement with the 56.7% predicted value based on independent estimates of individual contributors. The measured peak antenna efficiency for earlier data acquired at the 33.7 GHz KaBLE frequency (52.2%) is also in agreement with its predicted value (52.1%) [19].

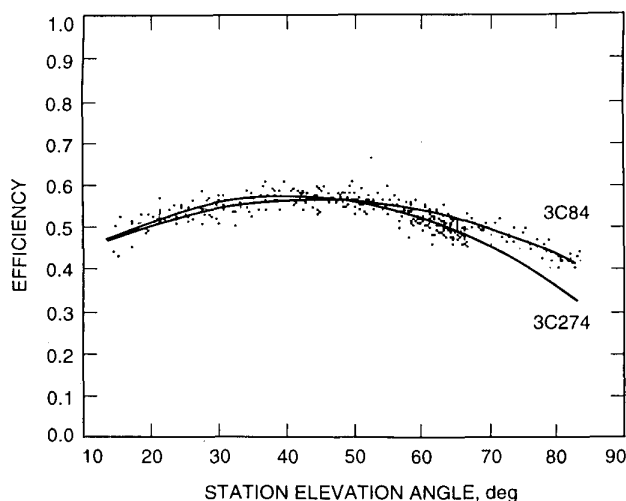


Figure 8. The antenna efficiency as a function of the elevation angle of the DSS-13 BWG antenna at Ka band (32.0 GHz), along with best-fit curves for 3C274-only data and 3C84-only data.

Figure 8 displays the Ka-band data, along with the 3C274 and the 3C84 best-fit curves. The northern-passing 3C84 high-elevation-angle antenna-efficiency measurements (maximum elevation of 84°) lie above those of 3C274 (maximum elevation of 67.2°). For the KaAP feed position in the DSS-13 pedestal room, the antenna efficiency is higher for sources with declinations greater than 35° that rise and set in the north. The increased spread in the data between sources is attributed to a dependence of the antenna efficiency due to probable misalignments in the beam-waveguide mirrors. This behavior is similar to that noted by Alvarez et. al. [20] for Ka-band measurements acquired at another BWG antenna, located in the Goldstone complex.

The measured Ka-band efficiencies show no significant variation with azimuth after removing the elevation-angle dependence from the data. This is consistent with the conclusion noted by other investigators [8].

The radio sources used for the Ka-band antenna-efficiency determination discussed above were the primary calibrator 3C274, and the variable source 3C84 (used primarily for curve shape). The planets Venus and Jupiter were observed for several passes performed during earlier 33.7 GHz sessions. The peak antenna efficiency of the Venus data, using $T_B = 461$ K in Table 2, was 7.3% below that of the 3C274 data. If the peak antenna efficiency using Venus data is scaled to match that of 3C274 data, the resulting $T_B = 430$ K still lies within the $1-\sigma$ uncertainty of the Steffes et. al. emission spectrum [17]. Possible contributions to this discrepancy include errors in the relative flux calibration of Venus and 3C274, errors due to significant brightness-temperature variation with phase angle [21], and modeling uncertainty in estimating the source-size correction of a planet. For the Jupiter data, using T_B given in Table 2, the estimated peak antenna efficiency was 1.5% below that using 3C274 data, which is within the 5% quoted uncertainty.

The gravity-induced roll-off of the antenna-efficiency curve, extrapolated to a 6.6° elevation angle (33.8° below the elevation angle of peak antenna efficiency), shows a projected degradation of

about 1.4 dB (using 3C274 data). Holography performed at 46.5° and 12.7° elevation predicts a 2 dB degradation between these two points. The estimated 1.4 dB degradation of the KaAP curve is consistent with the 2 dB holographic prediction, as there is a large uncertainty in extrapolating the (3C274 only) KaAP curve to an elevation angle (6.64°) where there are no data. At 20° elevation, the estimated 52.8% antenna efficiency corresponds to a degradation of 0.35 dB relative to the peak 57.2% value.

During certain passes, anomalous data points were observed (1) when the measured wind speeds exceeded 20 mph and the antenna was pointed directly into the direction of the oncoming wind, or (2) when the wind speed exceeded 30 mph. The majority of these data points were automatically removed, due to the magnitude of the AUTOBORE pointing offsets exceeding a set 2 mdeg tolerance. Cases where the pointing errors were acceptable but the measured efficiencies were suspect occurred during periods of significant gain variations, and were thus deleted. A possible cause of the large gain variations is insufficient isolation of the pedestal-room environment from significant outside weather changes. Data from passes that occurred during especially turbulent weather including periods of rain have also been removed due to the breakdown of the boresight algorithm in response to the large atmospheric variations in T_{op} .

The rms scatter of the data about the fitted polynomials provides a measure of the noise in the data. For 3C274-only data, the rms scatter (1.6%) agrees well with that of 3C84-only data (1.7%). The major contributors to this scatter are expected to be radiometer-gain instability, atmospheric-noise variations, and error in determination of the atmospheric loss factors used to refer the measurements to zero atmosphere. Measured values of gain instability from radiometer calibration data are consistent with the 1.0% rms scatter of data acquired from a single source during a single pass, suggesting that radiometer gain fluctuation is the dominant error source during these "good" weather passes.

The higher amount of scatter for the full data set combined over the several different passes, 1.6%, is likely due to differences in how accurately the atmospheric-loss corrections, L_{atm} , can be

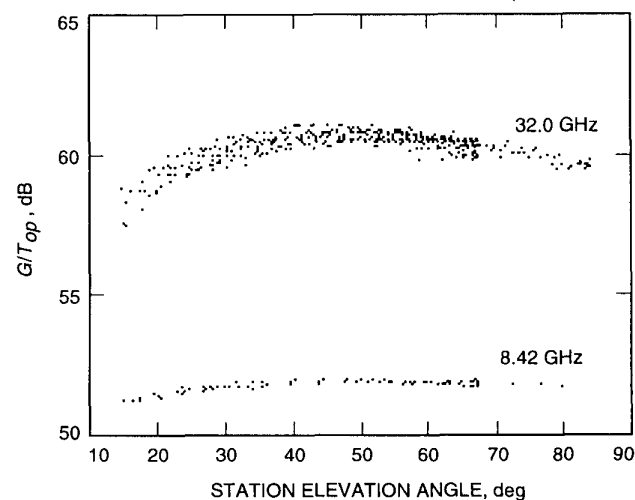


Figure 9. The G/T_{op} figure-of-merit as a function of the elevation angle of the DSS-13 BWG antenna at X band (8.4 GHz) and Ka band (32.0 GHz).

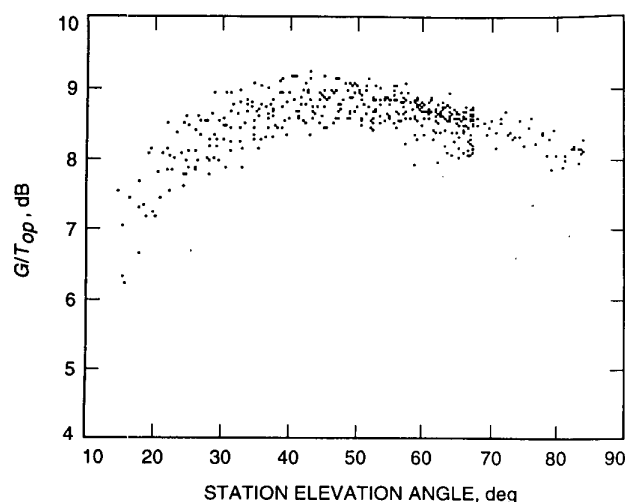
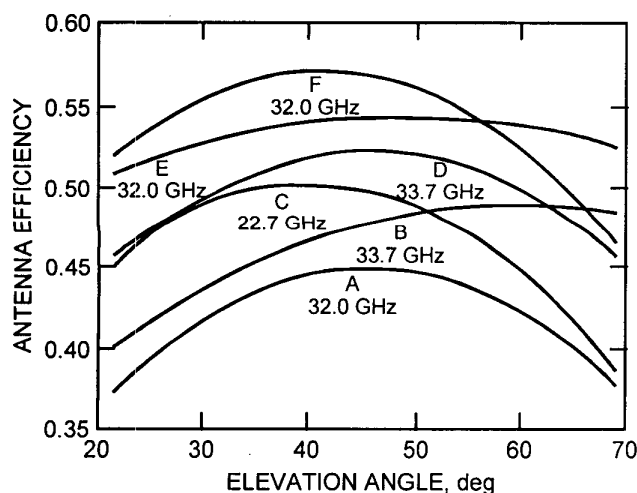


Figure 10. The G/T_{op} ground-station advantage (Ka band over X band) as a function of elevation angle of the DSS-13 BWG antenna.



LEGEND		
CURVE	MEASUREMENT EPOCH	ϵ_{pk} , %
A	1/1991	44.9
B	12/1993–1/1994	48.8
C	2/1994–9/1994	50.1
D	9/1994	52.2
E	11/1994–12/1994	54.3
F	2/1995–11/1995	57.1

Figure 11. The history of Ka-band performance measurements at DSS-13: the Ka-band antenna efficiency as a function of the elevation angle.

determined from one pass to the next. The atmospheric-loss factor is usually determined from a single tipping curve measurement, either at the start or end of a pass.

5.3 G/T_{op} performance

The G/T_{op} figure-of-merit characterizes the ground station contribution used in link studies by spacecraft-mission planners. Figure 9 is the G/T_{op} estimated from the data at both frequencies, using Equation (7). The relative link advantage of Ka band over X band plotted in Figure 10 is the Ka-band G/T_{op} data point in Figure 9, differenced from the value fitted over the X-band data points at the observed Ka-band data-point elevation angle. From Figure 10, we see a 7 to 9 dB advantage of Ka band relative to X band for the current station configuration. However, if both Ka-band and X-band G/T_{op} measurements are adjusted using the projected noise temperatures of improved HEMT LNAs [22], the resulting ground-link advantage lies between the expected 6 to 8 dB.

5.4 History of DSS-13 BWG performance improvements at Ka band

Since the DSS-13 BWG antenna was first placed into operation, in 1990, a series of performance improvements have been implemented. Figure 11 displays each curve that was fit from the measured Ka-band antenna-efficiency data acquired between these configuration changes. Note the progressive improvement in peak antenna efficiency as each configuration change was implemented.

Curve A in Figure 11 is the antenna-efficiency curve measured in January, 1991, during DSS-13's first configuration at 32 GHz, as part of its post-construction performance evaluation [22]. The data for this curve were acquired using a test package located at a different F3 feed position in the DSS-13 pedestal room. Initial theodolite and holography panel-setting sessions were conducted in August-September, 1990, resulting in 0.42 mm normal rms surface error of the main reflector [24].

In January, 1992, the panels were readjusted, with a resulting normal rms surface error of 0.38 mm. Other activities that occurred during the interim between curves A and B were the stiffening of the turntable platform of the ellipsoidal mirror in the pedestal room used to direct the incoming RF energy to the desired feed position, and the removal of a bypass feed shroud, which was used for early testing of the antenna.

The first KaAP sessions were conducted between December, 1993, and January, 1994, at the KaBLE frequency of 33.7 GHz. These data produced a peak measured antenna efficiency of 48.8% at 59.5° elevation (curve B). The net improvement of the curve B peak efficiency over that of curve A was found to be consistent with the expected improvement, after taking into account all known configuration differences between the two sessions. However, as seen in Figure 11, curve B is peaked significantly away from the 45° rigging angle, at about 60°. This was caused by the stiffening of the ellipsoid's support structure, with no follow-up mirror-alignment activity.

The January-February, 1994, holography session included adjustment of the panels in the outer two rings of the main reflector, resulting in an improved normal rms surface error of 0.31 mm.

In addition, a series of mirror-alignment operations[25] were conducted to move the peak of the antenna efficiency curve nearer 45°. This next series of measurements (curve C) (February-September, 1994) yielded a peak antenna efficiency of 50.1% at an elevation angle of 39.5°.

In September, 1994, a manual adjustment in the subreflector lateral x position of 0.2 in was made. A small data set taken shortly after showed a small improvement, with a peak antenna efficiency of 52.2% at 45.4° (curve D).

In October, 1994, the KaAP Ka-band system was modified to receive the standard DSN allocated frequency band at 32.0 GHz (replacing the KaBLE 33.7 GHz system). At the same time, additional subreflector lateral x-position adjustments were made, and a new subreflector look-up table was installed. The resulting November-December, 1994, data set at 32.0 GHz showed an improved peak antenna efficiency of 54.3% at 48.4° elevation angle, but with a significantly flattened curve (curve E). The expected improvement in peak antenna efficiency at 32.0 GHz should have been significantly greater (with the same curve shape). It was found that the subreflector optimization procedures, using low-resolution holography, had been performed at another feed position in the pedestal room at DSS-13. Upon checking the ellipsoid and subreflector at the KaAP position using radiometry, it was found that a significant additional 0.05 in subreflector z-position correction was required to increase the peak antenna efficiency [26]. The most recent data set (curve F in Figure 11), presented and discussed in Section 5.2, displays the improvement over curve E after applying this correction. The peak antenna efficiency of 57.1% occurs at 40.6° elevation angle. The measured improvement of 0.2 dB is consistent with the 0.14 dB improvement predicted from holography [27].

In late 1996, the HEMT Ka-band package was removed from the feed position, and other packages were installed for testing and demonstration purposes. Since February, 1997, a monopulse receiver has been in place, routinely acquiring KaAP natural radio source and Mars Global Surveyor (MGS) KaBLE-II spacecraft Ka-band data [6, 7].

6. Conclusion

The KaAP antenna-efficiency measurements acquired at the DSS-13 R&D beam-waveguide antenna, conducted between December, 1993, and November, 1995, have been presented. This on-going effort was continued in order to characterize the antenna-efficiency performance and Ka-band-over-X-band link advantage, and to supplement measurements acquired from spacecraft signals.

7. Acknowledgements

I would like to thank W. Imbriale, J. Layland, R. Clauss, C. Stelzried, C. Edwards, D. Rochblatt, D. Bathker, and M. Klein for many informative discussions and comments; the DSS-13 station personnel for conducting the experiments and acquiring the data (G. Bury, C. Goodson, L. Smith, G. Farner, R. Reese, R. Littlefair, J. Crook, J. Garnica, L. Skjerve and L. Tanida); E. Paulsen, M. Britcliffe, J. Bowen, V. Vilnrotter, and S. Stewart for providing information on equipment and station specifications; and T. Rebold for assistance in software development. The research described in this paper was carried out by the Jet Propulsion Laboratory, Cali-

fornia Institute of Technology, under a contract with the National Aeronautics and Space Administration.

8. References

1. J. W. Layland and L. L. Rauch, "The Evolution of Technology in the Deep Space Network: A History of the Advanced Systems Program," The Telecommunications and Data Acquisition Progress Report 42-130, April-June 1996, Jet Propulsion Laboratory, Pasadena, California, August 15, 1997, pp. 96-103.
2. J. G. Smith, "Ka-Band (32 GHz) Downlink Capability for Deep Space Communications," The Telecommunications and Data Acquisition Progress Report 42-88, October-December 1986, Jet Propulsion Laboratory, Pasadena, California, February 15, 1987, pp. 96-103.
3. J. W. Layland and J. G. Smith, "A Growth Path for Deep Space Communications," The Telecommunications and Data Acquisition Progress Report 42-88, October-December 1986, Jet Propulsion Laboratory, Pasadena, California, February 15, 1987, pp. 120-125.
4. A. L. Riley, D. M., Hanson, A. Mileant, and R. W. Hartop, "A Ka-Band Beacon Link Experiment (KABLE) with Mars Observer," The Telecommunications and Data Acquisition Progress Report 42-88, October-December 1986, Jet Propulsion Laboratory, Pasadena, California, February 15, 1987, pp. 141-147.
5. T. A. Rebold, A. Kwok, G. E. Wood, and S. Butman, "The Mars Observer Ka-Band Link Experiment," The Telecommunications and Data Acquisition Progress Report 42-117, January-March 1994, Jet Propulsion Laboratory, Pasadena, California, May 15, 1994, pp. 250-282.
6. D. D. Morabito, S. Butman, and S. Shambayati, "Recent Results from the Mars Global Surveyor Ka-band Link Experiment (MGS/KaBLE-II)," Proceedings of the Fourth Ka-Band Utilization Conference, November 2-4, 1998, Venice, Italy (IIC-Istituto Internazionale delle Comunicazioni, Via Perinace-Villa Piaggio, 16125 Genova, Italy), pp. 365-372.
7. S. Butman, D. D. Morabito, A. Mittskus, J. Border, J. Berner, C. Whetsel, M. Gatti, C. Foster, V. Vilnrotter, H. Cooper, A. Del Castillo, A. Kwok, J. Weese, M. Speranza, R. David, W. Adams, A. McMeichen, C. Goodson, G. Bury, and D. Reece, "The Mars Global Surveyor Ka-Band Link Experiment (MGS/KaBLE-II)," *Proceedings of Third Ka-Band Utilization Conference and International Workshop on SCGII*, September, 1997, Naples, Italy (F. Bertoldi, Istituto Internazionale delle Comunicazioni, Genova, Italy), pp. 179-186.
8. W. A. Imbriale, M. S. Esquivel, and F. Manshadi, "Novel Solutions to Low-Frequency Problems With Geometrically Designed Beam-Waveguide Systems," The Telecommunications and Data Acquisition Progress Report 42-122, April-June 1995, Jet Propulsion Laboratory, Pasadena, California, August 15, 1995, pp. 138-150.
9. L. S. Alvarez, "Analysis and Applications of a General Bore-sight Algorithm for the DSS-13 Beam Waveguide Antenna," The Telecommunications and Data Acquisition Progress Report 42-111, July-September 1992, Jet Propulsion Laboratory, Pasadena, California, November 15, 1992, pp. 48-61.

10. J. C. Chen, P. H. Stanton, and H. F. Reilly, "Performance of the X/Ka-/KaBLE-Band Dichroic Plate in the DSS-13 Beam Waveguide Antenna," The Telecommunications and Data Acquisition Progress Report 42-115, July-September, 1993, Jet Propulsion Laboratory, Pasadena, California, November 15, 1993, pp. 54-64.
11. J. Bowen and D. Neff, "A Cryogenic Seven Element HEMT Front End for DSS-13," The Telecommunications and Data Acquisition Progress Report 42-114, April-June, 1993, Jet Propulsion Laboratory, Pasadena, California, August 15, 1993, pp. 51-60.
12. C. T. Stelzried, and M. J. Klein, "Precision DSN Radiometer Systems: Impact on Microwave Calibrations," *Proceedings of the IEEE*, **82**, May 1994, pp. 776-787.
13. S. J. Keihm, "Water Vapor Radiometer Measurements of the Tropospheric Delay Fluctuations at Goldstone Over a Full Year," The Telecommunications and Data Acquisition Progress Report 42-122, April-June 1995, Jet Propulsion Laboratory, Pasadena, California, August 15, 1995, pp. 1-11.
14. D. D. Morabito, R. Clauss, and M. Speranza, "Ka-Band Atmospheric Noise-Temperature Measurements at Goldstone, California, Using a 34-Meter Beam-Waveguide Antenna," The Telecommunications and Data Acquisition Progress Report 42-132, October-December 1997, Jet Propulsion Laboratory, Pasadena, California, February 15, 1998, pp. 121-152.
15. P. Richter, "Radio Source List for Antenna Calibration," DSN No. 890-269, October 15, 1994, JPL Doc. No. D-3801 (JPL internal document), Jet Propulsion Laboratory, California Institute of Technology.
16. M. Klein, personal communication, Jet Propulsion Laboratory, Pasadena, California, February 3, 1994.
17. P. G. Steffes, M. J. Klein, and J. M. Jenkins, "Observations of Microwave Emission of Venus from 1.3 to 3.6 cm," *Icarus*, **84**, 1990, pp. 83-92.
18. I. de Pater, and S. T. Massie, "Models of the Millimeter-Centimeter Spectra of the Giant Planets," *Icarus*, **62**, 1985, pp. 143-171.
19. D. D. Morabito, "The Efficiency Characterization of the DSS-13 34-Meter Beam-Waveguide Antenna at Ka-Band (32.0 and 33.7 GHz) and X-band (8.4 GHz)," The Telecommunications and Data Acquisition Progress Report 42-125, January-March 1996, Jet Propulsion Laboratory, Pasadena, California, May 15, 1996, pp. 1-20.
20. L. S. Alvarez, M. J. Britcliffe, M. M. Franco, S. R. Stewart, and H. J. Jackson, "The Efficiency Calibration of the DSS-24 34-Meter Diameter Beam-Waveguide Antenna," The Telecommunications and Data Acquisition Progress Report 42-120, October-December 1994, Jet Propulsion Laboratory, Pasadena, California, February 15, 1995, pp. 174-187.
21. L. del Ciampo, "Centimeter Emission Variation of Venus," Masters thesis in Space Science/Radioastronomy and Solar Physics, Instituto de Pesquiass Espaciais, October 1989.
22. J. Shell, personal communication, Jet Propulsion Laboratory, Pasadena, California, June 12, 1995: $T_{LNA}(X) = 6\text{ K}$; $T_{LNA}(Ka) = 13\text{ K}$.
23. S. D. Slobin, T. Y. Otsoshi, M. J. Britcliffe, L. S. Alvarez, S. R. Stewart, and M. M. Franco, "Efficiency Measurement Techniques for Calibration of a Prototype 34-Meter-Diameter Beam-Waveguide Antenna at 8.45 and 32 GHz," *IEEE Transactions on Microwave Theory and Techniques*, **MTT-40**, 6, June 1992, pp. 1301-1308.
24. D. Rochblatt, J. Withington, B. Seidel, and H. Jackson, "Performance Improvement of DSS-13 at the Rigging Angle by Unbending the Panels in Rings 8 and 9," JPL IOM 3328-94-023 (JPL internal document), March 23, 1994.
25. R. Thomas, "DSS 13 Mirror Alignment," Planning Research Corporation Inc. memorandum, February 18, 1994.
26. V. Vlnrotter, personal communication, Jet Propulsion Laboratory, Pasadena, California, January 1995.
27. D. Rochblatt, personal communication, Jet Propulsion Laboratory, Pasadena, California, March 17, 1995.
28. P. Richter, personal communication, Jet Propulsion Laboratory, Pasadena, California, December 13, 1993.
29. M. Gatti, and M. Klein, personal communication, Jet Propulsion Laboratory, Pasadena, California, June 1994.

Introducing Feature Article Author



David D. Morabito was born in Los Angeles, California, on January 27, 1952. He did his undergraduate and graduate work in Electrical Engineering at the University of Southern California between 1970 and 1979. Since 1973, he has worked at Caltech's Jet Propulsion Laboratory in Pasadena, California, on several engineering and scientific research projects. Among the areas he has worked on are spacecraft navigation; very-long-baseline interferometry (VLBI); radio-science experiments for Voyager 2, Ulysses, Galileo, and Mars Observer; antenna-performance characterization of beam-waveguide antennas; atmospheric-noise effects on spacecraft links; and design work on telecommunications systems for future space missions. His most recent project is studying the use of Ka band as a telecommunications link frequency for spacecraft communications. He has over sixty publications in several professional journals and conference proceedings. He is a member of the IEEE, the American Astronomical Society, and the American Geophysical Union. ☞